Published in final edited form as:
Microvasc Res. 2013 March ; 86: 1–10. doi:10.1016/j.mvr.2012.12.001.

Novel 3D analysis of Claudin-5 reveals significant endothelial heterogeneity among CNS microvessels

Debayon Paul[1], **Ann E. Cowan**[2], **Shujun Ge**[1], and **Joel S. Pachter**[1,*]

[1]Blood-Brain Barrier Laboratory, Department of Cell Biology, University of Connecticut Health Center, 263 Farmington Ave., Farmington, CT 06030

[2]Center for Cell Analysis and Modeling, Department of Molecular, Microbial & Structural Biology, University of Connecticut Health Center, 263 Farmington Ave., Farmington, CT 06030

Abstract

Tight junctions (TJs) feature critically in maintaining the integrity of the blood-brain barrier (BBB), and undergo significant disruption during neuroinflammatory diseases. Accordingly, the expression and distribution of CLN-5, a prominent TJ protein in central nervous system (CNS) microvessels and BBB determinant, has been shown to parallel physiological and pathophysiological changes in microvascular function. However, efforts to quantify CLN-5 within the CNS microvasculature *in situ*, by using conventional two-dimensional immunohistochemical analysis of thin sections, are encumbered by the tortuosity of capillaries and distorted diameters of inflamed venules. Herein, we describe a novel contour-based 3D image visualization and quantification method, employing high-resolution confocal z-stacks from thick immunofluorescently-stained thoracolumbar spinal cord cryosections, to analyze CLN-5 along the junctional regions of different-sized CNS microvascular segments. Analysis was performed on spinal cords of both healthy mice, and mice experiencing experimental autoimmune encephalomyelitis (EAE), an animal model of the neuroinflammatory disease multiple sclerosis. Results indicated that, under normal conditions, the density of CLN-5 staining (CLN-5 intensity/endothelial surface area) was greatest in the capillaries and smaller venules, and least in the larger venules. This heterogeneity in junctional CLN-5 staining was exacerbated during EAE, as spinal venules revealed a significant loss of junctional CLN-5 staining that was associated with focal leukocyte extravasation, while adjacent capillaries exhibited neither CLN-5 loss nor infiltrating leukocytes. However, despite only venules displaying these behaviors, both capillaries and venules evidenced leakage of IgG during disease, further underscoring the heterogeneity of the inflammatory response in CNS microvessels. This method should be readily adaptable to analyzing other junctional proteins of the CNS and peripheral microvasculature, and serve to highlight their role(s) in health and disease.

*Corresponding author pachter@nso1.uchc.edu, tel.: 860-679-3698, fax: 860-679-1269.

Competing interests
The authors have no competing interests.

Keywords

EAE; Blood-brain barrier; Endothelial heterogeneity; Claudin-5; Volume rendering; Isosurface rendering

Introduction

Significant restriction of paracellular movement of soluble substances between the central nervous system (CNS) parenchyma and systemic circulation is one of the properties conferred by the blood-brain barrier (BBB). Such limitation is generally considered to derive from an intricate circumferential network of specialized membrane contacts, tight-junctions (TJs), which exist between CNS microvascular endothelial cells. For recent reviews on TJ regulation of paracellular solute flux and contribution to the BBB, see Furuse (2010), Blasig and Haseloff (2011), and Coisne and Engelhardt (2011).

The integrity of the BBB has been reported to be compromised during neuroinflammatory and neurodegenerative diseases, with disruption of TJs widely thought to contribute significantly to pathology (Petty and Lo, 2002; Hawkins and Davis, 2005; Carvey et al., 2009; Coisne and Engelhardt, 2011; Grammas et al., 2011). Some reports have noted that dysregulated expression, dephosphorylation and/or redistribution of TJ proteins at the BBB precede signs of clinical disease (Morgan et al., 2007; Argaw et al., 2009; Bennett et al., 2010). Such findings have been interpreted that alterations in TJs play a *causativ*e role in the inflammatory process. In this regard, disruption of TJs might facilitate leukocyte diapedesis through weakened interendothelial contact points (Garrido-Urbani et al., 2008), and/or support extravasation of serum proteins to which leukocytes must attach to invade the CNS parenchyma (Pober and Sessa, 2007). Additional reports have pointed to TJ disruption and associated BBB damage as being a *consequence* of the leukocyte diapedesis process itself –– particularly through the actions of leukocyte-derived matrix metalloproteinases and reactive oxygen species (Gidday et al., 2005; Pun et al., 2009; Moxon-Emre and Schlichter, 2011). And still others have found intermediate ground by linking opening of TJs to initial intimate contact between activated/infected leukocytes and the brain microvascular endothelium (Haorah et al., 2005; Suidan et al., 2008; Ivey et al., 2009). These interpretations are not mutually exclusive, and one mechanism may foster the others leading to protractive BBB dysfunction, TJ disruption, and a degenerative sequence of neurologic sequelae (Carvey et al., 2009).

TJs in the CNS are mainly comprised of three distinct families of integral membrane proteins, namely, occludin, junctional adhesion molecules A, B and C, and claudins (CLNs) – of which there are now more than 20 recognized isoforms in various endothelial and epithelial beds (Liebner et al., 2011; Paolinelli et al., 2011). In turn, these integral proteins are linked to the actin cytoskeleton through several scaffolding proteins, including zonula occludens (ZO) proteins 1, 2 and 3 (Hawkins and Davis, 2005; Abbott et al., 2006), which assist in regulating TJ performance and BBB phenotype through a variety of signal transduction cascades (Ishizaki et al., 2003; Fischer et al., 2005; Haorah et al., 2005; Zhong et al., 2008; Jalali et al., 2010; Morin-Brureau et al., 2011; Ma et al., 2012).

CLN-5 has been localized to endothelial cell junctions of CNS microvessels *in situ* (Morita et al., 1999; Wolburg et al., 2003; Dobrogowska and Vorbrodt, 2004; Sheikov et al., 2008) and *ex vivo* (Bake et al., 2009), as well in culture (Song and Pachter, 2003; Calabria et al., 2006; Nakagawa et al., 2009; Gesuete et al., 2011; Luissint et al., 2012). A critical role for CLN-5 in BBB function has further been established. Specifically, overexpression of CLN-5 in cultured brain microvascular endothelial cells was shown to heighten barrier properties

(Ohtsuki et al., 2007), while its deficiency imparted size-selective loosening of the BBB *in vivo* (Nitta et al., 2003). In order to correlate altered status of TJs with BBB dysfunction and disease processes, it is thus imperative to be able to accurately assess expression and distribution of TJs proteins such as CLN-5 at the BBB *in situ*.

While two-dimensional (2D) assessment of immunofluorescent confocal images obtained from thin sections of CNS tissue has revealed apparent changes in the amount and distribution of TJ proteins with neuroinflammatory disease (Persidsky et al., 2006; Alvarez and Teale, 2007; Argaw et al., 2009), this approach is limited in scope as it is restricted to visualization of only a minor fraction of any given vessel segment. Because of the severe tortuosity of CNS microvessels, 2D analysis of thin sections is largely confined to vessels of larger diameter, e.g., venules or arterioles, cut in cross-sectional profile (Janacek et al., 2011). Longitudinal profiles are not acquired to any significant extent by this tack and, therefore, much of the intercellular TJ network embedded within the long axis of the vascular wall is excluded from quantitative morphometric assessment. The information thus acquired may fail to capture highly focal changes in TJ expression/distribution. Moreover, cross-sections of the smaller diameter, but far more numerous, capillaries cannot accurately be evaluated for TJ expression as their circumference contains but only one to two cells. As endothelial heterogeneity may dictate that arterioles, capillaries, post-capillary venules and venules, differentially contribute to the BBB and inflammatory processes (Vorbrodt et al., 1986; Ge et al., 2005; Bechmann et al., 2007; Macdonald et al., 2010; Saubamea et al., 2012), it is possible that TJ responses and their physiological consequences are highly segment-dependent. Thus, it is important to be able to assay TJ expression qualitatively and quantitatively within all segment types along the CNS microvascular tree. It would further be advantageous to sample thicker tissue sections and access as much of the vascular surface as possible so as not to miss events that might be spatially restricted or polarized, and correlate TJ effects with those occurring in the perivascular spaces during inflammation such as step-wise penetration of leukocytes from lumen into the CNS parenchyma (Sixt et al., 2001; van Horssen et al., 2005).

With these considerations in mind, and using CLN-5 as an example, herein we describe a protocol aimed at providing more accurate focal information, greater resolution and enhanced spatial perspective regarding junctional TJ proteins during CNS inflammation. Specifically, expression of CLN-5 was analyzed by subjecting microvessels in thick sections to 3D rendering, yielding both qualitative and quantitative information about the status of BBB integrity, and its relationship to inflammatory disease. Using this protocol to analyze CNS tissue from mice inflicted with experimental autoimmune encephalomyelitis (EAE), an animal model for multiple sclerosis (Mix et al., 2010; Batoulis et al., 2011), examples are presented to show alterations in the amount and distribution of CLN-5 at inter-endothelial junctions of spinal cord microvessels, and how these changes correlate with other vascular manifestations of inflammation.

Materials and methods

EAE induction

Female C57BL/6J mice (Charles River Laboratories), age 8 – 10 weeks, were used throughout. All animal protocols were in compliance with Animal Care and Use Guidelines of the University of Connecticut Health Center (Animal Welfare Assurance # A3471-01). Active EAE was induced as recently described (Murugesan et al., 2012), following a modification of the procedure ofSuen et al. (1997). Subcutaneous flank injection of 300μg MOG35-55 peptide (MEVGWYRSPFSRVVHLYRNGK; synthesized by the Keck Biotechnology Resource Center at Yale University) in complete Freund's adjuvant (Difco) containing 300μg *M. tuberculosis* was performed on day 0 (d0), and supplemented by

intraperitoneal injections of 500ng pertussis toxin (List Biological) on d0 and d2. The typical disease that results from this protocol is monophasic, with acute symptoms beginning ~d10 – d12, and peak clinical disease appearing by ~d15 – d20, associated with ascending paralysis. Chronic disease then continues with disability achieving a plateau or diminishing somewhat by d25. The mice were scored on a scale of 0 to 5 with gradations of 0.5 for intermediate scores: 0, no clinical signs; 1, loss of tail tone; 2, wobbly gait; 3, hind limb paralysis; 4, hind and fore limb paralysis; and 5, moribund.

Tissue preparation

At designated times post-EAE induction, mice were anesthetized with ketamine (80 mg/kg, ip) and xylazine (10 mg/kg, ip) in phosphate buffered saline, pH 7.4 (PBS). Following exposure of the heart by left anterolateral thoracotomy, the mouse was transcardially perfused (via the left ventricle) first with Heparin-PBS (10 usp/ml), to flush out the blood, and then with fixation buffer (4% paraformaldehyde in 0.1 M phosphate buffer, pH 7.4), using an “in-house” constructed gravity perfusion apparatus.

Laminectomy was performed for harvesting the spinal cord. Briefly, the entire spinal column containing the spinal cord was removed and, after clearing the overlying ligaments and muscle, was incubated in fixation buffer for 2 hours at room temperature. The lamina was then ectomized by opening the spinal canal from the C1 to L5 vertebra, breaking one at a time using a pair of fine laminectomy forceps. The dissected spinal cords were post-fixed again in fixation buffer for 30 min, and then cryoprotected in 30% sucrose in 0.1M phosphate buffer, pH 7.4, overnight at 4°C prior to freeze-embedding in cryomatrix. Subsequently, 12×60μm cryosections were obtained from the thoracolumbar region, approximately between the T10 and L3 vertebrae (Fig. 1c), using a Thermo Fisher Scientific microtome (maintained at −25°C), and adhered to poly-L-lysine coated slides.

Immunostaining

Sections were permeabilized with 1% Triton X-100 in PBS for 30 min, and nonspecific binding blocked by incubation with Powerblock® in UltraPure™ (GIBCO) distilled water for 10 min. The microvascular endothelium was stained by rat anti-mouse CD31 (BD Pharmingen; 1:100 dilution) followed by incubation with goat anti-rat Alexa® 555 (Life Technologies; 1:200). The basement membranes were labeled with rabbit anti-mouse Laminin 1 (Cedarlane; 1:100) and goat anti-rabbit Alexa® 555 (Life Technologies; 1:200). Anti-mouse Claudin5-Alexa® 488 (Biolegend; 1:150) was employed to highlight the TJs at the interendothelial borders. Anti-mouse IgG-Alexa® 488 or IgG-Alexa® 555 F_{ab}, fragment (Life Technologies; 1:200) was utilized to detect the leaked endogenous serum IgG from inflamed CNS microvessels. Anti-mouse CD4-Alexa® 488 antibody (generously provided by Dr. H. E. de Vries, VU medical center, Netherlands) was used to immunolabel the perivascular leukocytes associated with inflamed microvessels. Additionally, nuclear stain DRAQ5 (Biostatus Ltd., Leicestershire, UK) was utilized to reveal the perivascular cellularity surrounding inflamed CNS microvessels due to leukocyte extravasation. Sections were mounted in Mowiol®.

Image acquisition

Spinal cord microvessels (capillaries and venules) from the dorsolateral white matter (between T10 and L3) were imaged and categorized into appropriate segments based on their average diameter (Fig 1. a-c). This region, just underneath the meninges, was intentionally selected for analysis as it sustains the earliest inflammation in the spinal cord parenchyma in the MOG35-55 EAE model (Brown and Sawchenko, 2007). Confocal z-stacks were acquired (at 1μm increments between z-slices) following a multitrack scan, using a Zeiss LSM 510 Meta confocal microscope equipped with a 40X Zeiss Fluar (NA

1.3, determining voxels of 0.62×0.62×1 μm^3) and a 63X Plan-neofluar (NA 1.25, determining voxels of 0.39×0.39×0.51 μm^3) oil immersion objective lens. Stitching of z-stacks from overlapping regions (in x, y plane) of the same vessel was performed by XuV stitch v1.8 software (Free Software Foundation Inc., Boston, USA).

3D quantification of microvascular CLN-5 density

To quantify relative CLN-5 protein expression within select microvessels, confocal zstacks were imported into Imaris® suite version 7.1 x64 software (Bitplane Inc., South Windsor, CT). Fluorescence intensities above a background value were assigned for each color channel in the volume rendered image (i.e., 3D reconstruction) and kept constant for all the acquired z-stacks. For quantification in 3D, manual contour tracing was first performed by cursoring out the vessel of interest in each confocal z-slice and the individual contours merged into a 3D contour surface. Surface area of the generated 3D contour was used as an estimate of the "microvascular surface area" defined by the endothelial layer. This 3D contour surface was subsequently used as a mask to isolate only the microvessel of interest from rest of the dataset by setting all voxel intensities "outside" the 3D contour surface to zero. The CLN-5 channel was isosurface rendered using surface creation wizard and the density of CLN-5 calculated as follows:

$$\text{Total CLN-5 intensity} = \text{Mean CLN-5 intensity} \times \#\text{ of voxels}$$

$$\text{CLN-5 intensity per unit area } (\textit{i.e., CLN-5 density}) = \frac{\text{Total CLN-5 intensity}}{\text{Microvascular surface area}}$$

In effect, this method allowed the surface area of the microvascular endothelium to be spread out in 3D space (x, y, z axes) for quantification of CLN-5 density per unit area (Fig 1. d-e), while excluding the luminal volume (Suppl. Fig. 1a-b).

Re-slicing isosurface-rendered images

The Clipping Plane module on Imaris® was employed to optically "re-slice" 3D isosurface rendered microvessels along a desired *oblique* plane, in a manner perpendicular to axis of the microvessel, so as to uncover hidden views and resolve the *interior* versus *exterior* or *luminal* versus *abluminal* vascular compartments. This tool further allowed resolution of the microvascular basement membrane into its endothelial and parenchymal counterparts, which split apart during neuroinflammation to accommodate the CNS invading leukocytes (Engelhardt and Sorokin, 2009).

To introduce the clipping plane tool into the 3D dataset, its icon in the object list was selected and the clipping plane first placed along a desired orthogonal plane (xy, yz or xz) with the manipulator (Suppl. Fig. 1). To further orient the clipping plane in an oblique plane, and align it perpendicular to axis of the microvessel for a cross-sectional view, the manipulator was selected and rotated as required. Finally, to alter the location of the clipping plane along the same axis, and thereby obtain different depths within the vessel, the manipulator was re-positioned accordingly.

2D quantification of CLN-5 immunostaining

Background subtracted volume rendered confocal z-stacks of venules from thoraco-lumbar spinal cord were exported from Imaris® as tiff images for ImageJ based 2D quantification of mean CLN-5 pixel intensities along the interendothelial junctions. Relative intensity values corresponding to the level of CLN-5 immunostaining were measured over 30–50 ROIs, each defining 10×10 pixels, traced in a non-overlapping manner along the intercellular borders in each venule, as previously described (Song and Pachter, 2004). For inflamed venules from EAE mice, ROIs were sampled from regions with visible reduction in CLN-5 immunoreactivity, and displaying dense perivascular cellularity. For venules from naïve

mice, ROIs were randomly selected along the microvessel profile. Mean pixel values were then obtained by averaging the intensity values of all ROIs.

Statistical Analysis

All statistical analyses were performed employing GraphPad Prism 5 software (La Jolla, CA, USA). Microvascular CLN-5 density values obtained from Imaris® 3D image analysis were expressed as mean ± standard error of the mean (SEM). One-way analysis of variance (ANOVA) was employed to assess statistically significant differences in junctional CLN-5 density between microvascular segments from naïve and d24 EAE mice, followed by Bonferroni's multiple comparison post-hoc analysis. For assessing the relationship between CLN-5 density and microvessel diameter, a Pearson product-moment correlation coefficient was determined. Comparison of CLN-5 mean pixel intensity values from 2D images of venules from naïve versus d24 EAE mice was performed by one-tailed unpaired Students *t*-test. Results were considered significant at a $p \leq 0.05$.

Results

Segmental heterogeneity of CLN-5 density in naïve spinal cord microvessels

To initially determine if normal spinal cord microvessels demonstrate segmental heterogeneity with respect to CLN-5 density at endothelial junctions, spinal cord sections from naïve mice were immunostained for CLN-5. Isosurface rendering of high-resolution confocal z-stacks obtained from the different-sized microvascular segments were subjected to 3D quantification of endothelial CLN-5 density. Microvascular segments were classified as larger venules (>20 μm in diameter); smaller, possibly 'postcapillary' venules (10–20 μm in diameter); and capillaries (<10 μm in diameter). This classification was based primarily on a consensus of established size criteria (Simionescu and Simnionescu, 1977; Leeson et al., 1988; Fawcett, 1994; Ross and Pawlina, 2006), as there is no widely recognized marker that distinguishes postcapillary venules (Owens et al., 2008). The smaller venules were often seen connecting capillaries to larger venules, lending support to the smaller venules being postcapillary in nature. To further verify venule identity, 3D isosurface rendered datasets were re-sliced along a desired plane using the clipping plane module in Imaris® to analyze microvessels in cross section (Suppl. Fig. 1c). The presence of a smooth, non-puckered lumen lent to microvessels (>20 μm in diameter) being classified as venules rather than arterioles (Macdonald et al., 2010).

Isosurface rendered z-stacks of venules and capillaries revealed appreciable heterogeneity in endothelial CLN-5 density (CLN-5 staining intensity/μm^2 microvascular surface) in naïve mice (Fig. 2 a-f). Specifically, 3D quantification of CLN-5 density in larger venules yielded a significantly lower mean value than that found in smaller, venules (19.95±1.65 vs. 48.89 ±2.97, respectively). CLN-5 density in larger venules was also significantly lower (2-fold) than that in naïve capillaries (19.95±1.65 vs. 39.77±2.54, respectively). However, junctional density of CLN-5 was not statistically different between capillaries and the smaller diameter venules. These results suggest that, under normal conditions, the density of CLN-5 at endothelial junctions within CNS microvessels tends to vary inversely with microvessel diameter, being greatest in the capillaries and smaller venules, and least in the larger venules (Suppl. Fig. 3). Specifically, a significant negative linear correlation coefficient was established with a Pearson's correlation coefficient ($\boldsymbol{r}$) = −0.73.

Reduction of CLN-5 density in spinal cord venules during MOG-induced EAE

As MOG-induced EAE has been reported to result in diffuse TJ breakdown and relocalization of the TJ scaffolding protein ZO-1 in CNS microvessels (Bennett et al., 2010),

we evaluated if EAE affects junctional CLN-5 density equally in various microvascular segments (capillaries vs. venules) at the peak of disease.

Isosurface rendering of spinal cord venules at d24 EAE revealed significant disruption of CLN-5 distribution at sites of dense perivascular cellularity (Fig, 3a and 3b). These sites largely coincided with $CD4^+$ leukocyte infiltrates (Suppl. Fig. 2) and thus corroborated the vessels as inflamed. Moreover, there was considerable heterogeneity in junctional CLN-5 loss among venules – possibly reflecting a range in inflammatory status and/or vulnerability within this vessel population. The venules analyzed varied in diameter from ~20 – 50 m – a range shown to become inflamed in this and similar EAE paradigms (Pfeiffer et al., 2011; Bergman et al., 2012) – and thus could have included initially smaller, postcapillary venules that had distended in size due to disease. In keeping with the prior description that relocalization of the TJ scaffolding protein ZO-1 correlates with sites of inflammatory cell accumulation (Bennet et al., 2010), venules qualitatively showing near complete breakdown of CLN-5 staining pattern and displaying a CLN-5 density of <10 were considered to be *severely* inflamed. By contrast, those venules showing small punctate regions of CLN-5 loss and having a CLN-5 density of ≥10 were considered *moderately* inflamed. Capillaries in regions with even severely inflamed venules appeared refractory to CLN-5 loss (Fig. 3c). Specifically, quantification of junctional CLN-5 density revealed a 5-fold difference in severely inflamed venules compared to capillaries (4.79±0.78 vs. 24.0±5.85, respectively), while moderately inflamed venules and capillaries did not significantly differ in this measure (12.95±0.49 vs. 24.0±5.85, respectively). As the moderately inflamed venules displayed only small punctate regions of CLN-5 loss, it was unclear if they had yet to suffer diffuse extensive disruption, were less susceptible to disruption, or in stages of repair. As all size vessels analyzed in naïve mice clearly showed continuous CLN-5 staining along interendothelial borders in a 60 m section (Fig. 2), it is unlikely that the significant reduction in venular CLN-5 junctional density in EAE mice was due to obstacles to antibody penetration. Instead, it probably reflected a differential response in this vessel population.

Comparison of junctional CLN-5 density in inflamed venules from EAE mice and normal venules from naïve mice

Having first established the heterogeneity of CLN-5 density at endothelial junctions within the normal spinal microvasculature, and then within the diseased microvasculature during EAE, we next directly compared capillaries and venules from naïve and EAE mice. Results reveal that d24 EAE venules had significantly lower (~3.9 fold) CLN-5 density compared to both naïve venules (8.87±1.31 vs. 34.42±6.65, respectively) and naïve capillaries (8.87±1.31 vs. 34.74±3.70, respectively) (Fig. 4i). Additionally, there was no statistically significant alteration in CLN-5 density between the naïve and d24 EAE capillaries, or evidence of perivascular cellularity associated with capillaries during disease. These findings highlight that venules are the primary sites of neuroinflammation-associated junctional CLN-5 loss and possibly TJ breakdown, while capillaries appear to maintain their pattern of junctional CLN-5 immunoreactivity during EAE.

To confirm that our 3D analysis of CLN-5 density reflected diminished expression of the TJ protein at interendothelial junctions in venules during EAE, and not just redistribution of CLN-5 over a dilated, wider surface area, conventional 2D analysis of mean pixel intensity was performed along the intercellular junctional regions. Suppl. Fig. 4 shows that CLN-5 staining in inflamed venules from d24 EAE mice had significantly lower mean pixel intensity than that in venules of naïve subjects (~ 4.2-fold). The higher variability of CLN-5 staining during EAE, as indicated by both increased standard deviation and standard error of mean pixel intensity measure, were consistent with the more fragmented, irregular appearance of TJ staining associated with neuroinflammatory disease.

Heterogeneity of CLN-5 density in contiguous spinal cord microvessels during EAE

Though diverse inflammatory responses of closely located microvessels have provided strong evidence of segmental endothelial heterogeneity (Thurston et al., 2000; Xu et al., 2005), it isn't clear if venules and capillaries directly attached to each other show such disparity within the inflamed CNS. Therefore, a contiguous venule/capillary pair from a d24 EAE spinal cord section was subjected to 3D reconstruction and isosurface rendering for CLN-5 (Fig. 5a-b), to visualize segmental changes in CLN-5 density at the endothelial junctions. In what amounts to yet another clear display of segmental endothelial heterogeneity, a capillary emanating from a severely inflamed venule had intact junctional CLN-5 staining similar to that seen in capillaries of naïve mice. However, the immediately adjacent venule demonstrated near obliteration of CLN-5 junctional organization, along with separation of endothelial and parenchymal basement membranes and increased perivascular cellularity (Fig. 5a, insets). This finding reinforces the view that loss of junctional CLN-5 protein during neuroinflammation reflects an inherent susceptibility of CNS venules – a property not shared even by the most closely juxtaposed capillaries (Fig. 5c).

Heightened microvascular permeability to endogenous serum IgG occurs in both capillaries and venules during EAE

Given the disparate CLN-5 response between venules and capillaries during EAE, we next sought to determine if both microvessel types evidenced inflammation-associated leakage of serum IgGs. Thick spinal cord cryosections from both d6 (early stage) and d24 (late stage) EAE animals were stained for endogenous IgG and the basement membrane protein laminin-1 (Lam-1), followed by 3D reconstruction and isosurface rendering of the z-stacked confocal dataset (Fig. 6 a-d). IgG leakage was detected as focal deposits around both venules and capillaries at d6. Despite evidence of IgG extravasation at this early time, no loss of junctional CLN-5 was apparent (Suppl. Fig. 5). By d24, extravasation of IgG was so pronounced and diffuse that it obscured boundaries between the microvessel segments, though increased perivascular cellularity was associated with inflamed venules only (Fig. 6).

Discussion

Given the importance of TJs in neuroinflammatory disease, and increasing awareness of endothelial heterogeneity, this report described a novel microvascular contour-based 3D quantification method of acquiring and analyzing expression of the TJ protein CLN-5, a critical BBB determinant, along different type microvessel segments of the spinal cord during EAE. Venules were shown to display significant loss of CLN-5 at intercellular junctions during EAE, which was accompanied by severe extravasation of leukocytes and disruption of basement membrane integrity. In stark contrast, capillaries showed none of these responses.

This 3D approach also allowed for capture and analysis of small diameter capillaries lying in close proximity to venular structures. Due to their small caliber and tortuosity, such capillaries are typically precluded from conventional 2D analysis of TJs in thin-sectioned material. However, in the current protocol capillaries and venules directly attached to each other could be readily contrasted, allowing for a clearer picture of their diverse phenotypes in physiology and pathophysiology to emerge. In this regard, the density of CLN-5 expression under normal conditions was observed to vary inversely with microvessel diameter, being greatest in the capillaries and smaller venules, and least in the larger venules. That the correlation coefficient was −0.73, and not closer to −1.0, might reflect that CLN-5 density reaches asymptotes at the extreme diameters of the microvascular tree, and/or the 3D quantification approaches its limits of accuracy at these extremes. Nevertheless, this inverse relationship of CLN-5 density with diameter size was significant. This

discrepancy in CLN-5 density between capillaries and venules was further exaggerated during EAE, as loss of CLN-5 expression appeared restricted to venular structures. Loss of junctional CLN-5 might render the venular endothelium more amenable to leukocyte extravasation via the paracellular pathway (Garrido-Urbani et al., 2008). Alternatively, it could be the result of a sustained transendothelial leukocyte migration specifically at venular domains (Xu et al., 2005).

Despite the most significant CLN-5 loss being reserved for venules, IgG leakage was nevertheless detected around all size microvessels during early and late EAE. As capillaries did not sustain significant CLN-5 loss even as late as d24 EAE, this might reflect that inflammation-associated IgG leakage at these sites occurred primarily through transcytosis (Claudio et al., 1989; Proulx et al., 2012) – a process that, presumably, would not have required TJ breakdown (Kreuter, 2012). Venules, on the other hand, might have similarly employed IgG transcytosis early during EAE, but also engaged in paracellular leakage later following the extensive CLN-5 loss.

Xu et al. (2005) described similar breakdown of TJs and loss of CLN-1/3 and occludin at inter-endothelial contacts within retinal venules during a related condition, experimental autoimmune uveoretinitis. And in a further parallel with our results, they similarly reported retinal capillaries were apparently spared disruption of these TJ proteins – again highlighting endothelial heterogeneity and the differential endothelial response to inflammation. Using confocal microscopy of retinal whole mounts, this group has most recently elaborated a means to portray relative fluorescent intensity values of microvessel-associated CLN-1/3 in a 3D heat map (Xu and Liversidge, 2011). Our work extends these studies by employing 3D isosurface renderings of individual microvessels, thereby allowing a holistic perspective of TJ protein distribution within the microvascular network, in addition to enabling relative quantification. Furthermore, the acquisition of high-resolution confocal z-stacks from 60μm thick sections supported analysis of local effects, which in thinner sections or 2D analysis might well have been missed.

The d24 time-point of EAE was selected for analysis as it is soon after the apex of clinical disease in this particular paradigm (Suen et al., 1997), and into the chronic phase when inflammatory histopathology is at or near maximum (Pachner, 2011). Thereafter, clinical presentation either plateaus or abates somewhat. The spinal cord region between T10 and L3 vertebrae was the area of focus as disease commences at the lumbo-sacral level and progresses in the caudal-to-rostral direction (Gruppe et al., 2012). We thus reasoned that by the d24 time-point, maximal CLN-5 disorganization would be achieved at the spinal level analyzed. It is significant that IgG leakage was apparent from both capillaries and venules during early (d6) and late (d24) EAE, though no reduction in CLN-5 density was apparent in capillaries at either of these time-points. This scenario underscores a differential responsiveness between CNS capillaries and venules vis-à-vis neuroinflammation-associated changes in CLN-5 density at endothelial junctions. That C57 BL/6 mice display a similar overall CNS microvascular architecture and BBB transcriptome from mouse-to-mouse (Ward et al., 1990; Macdonald et al., 2010) perhaps contributed to the low variance in CLN-5 density within each group of microvessels analyzed, and aided in highlighting this heterogeneity.

Owing to the fact that microvascular density is greatly reduced in white matter compared to gray matter (Cavaglia et al., 2001), and venules constitute only a small percentage of the microvascular surface area (Berne and Levy, 1988), we were limited in the venule population to sample from the dorsolateral region. A further constraint was trying to capture venules with juxtaposed capillaries, so as to compare both basal and reactive CLN-5 expression by the two types of microvessel segments within the same or similar

microenvironment. Nonetheless, sampling of 12×60μm sections between T10 and L13 vertebrae enabled sufficient acquisition of venules/capillaries for statistical comparisons, while minimizing differences in endothelial phenotype due exclusively to regional heterogeneity within the CNS (Ge et al., 2005).

In contrasting TJ protein during health and disease, and between different microvessel subtypes, we chose to express the density of CLN-5 expression in relation to microvessel surface area rather than microvessel volume, as volume ($\pi r^2 h$) increases with the square of the radius of a cylinder. As the lumen – which is 'dead space' – disproportionately contributes more to the vascular volume of bigger segments, reporting TJ protein density per unit volume would yield artifactually lower values in larger diameter vessels even if the number of TJ proteins per unit area of endothelial membrane were unaltered from vessel to vessel. This is important not only for comparing different vessel subtypes in healthy subjects, but also when evaluating changes in any one vessel subtype during disease, as vessel caliber may swell along with the separation of basement membranes. We recognize, however, individual endothelial cells of larger diameter vessels may also be bigger than in the smallest capillaries, and that this could also lend toward a skewing of TJ protein density data being highest in the smaller vessels. It is nevertheless significant that Nagy et al., (1984) reported that the 'complexity' of brain TJ protein particles; i.e., the degree to which they comprise long, uninterrupted strands when viewed in freeze-fracture faces, is highest at the capillary end of the vascular tree and much less so at the venular end. Thus, our method of analysis yielded results consistent with the freeze-fracture technique, which displayed the *en face* vista of the interior of the cell membrane and focused exclusively at the intercellular junctions. That the reduced CLN-5 density in venules during EAE reflects diminished protein expression and not just dilation-associated distortion in endothelial cell size, is reinforced by our observations of reduced mean pixel intensity of CLN-5 immunostaining along the venular endothelial junctions during EAE, and the recent report describing loss of CLN-5 protein in EAE brain (Errede et al., 2012), as evidenced by Western blotting and quantitative optical densitometry. The current method should thus have broad applications in efforts to link changes in the expression and/or distribution of TJ proteins with focal microvascular incidents in the CNS and peripheral tissues.

Supplementary Material

Refer to Web version on PubMed Central for supplementary material.

Acknowledgments

We are grateful to Dr. H. E. de Vries for providing the CD4-Alexa® 488 antibody. This work was supported in part by grants 5RO1NSO61525-11 from the National Institutes of Health and RG 4503A4/1 from the National Multiple Sclerosis Society to J.S.P.

References

Abbott NJ, et al. Astrocyte-endothelial interactions at the blood-brain barrier. Nat Rev Neurosci. 2006; 7:41–53. [PubMed: 16371949]

Alvarez JI, Teale JM. Evidence for differential changes of junctional complex proteins in murine neurocysticercosis dependent upon CNS vasculature. Brain Res. 2007; 1169:98–111. [PubMed: 17686468]

Argaw AT, et al. VEGF-mediated disruption of endothelial CLN-5 promotes blood-brain barrier breakdown. Proc Natl Acad Sci U S A. 2009; 106:1977–1982. [PubMed: 19174516]

Bake S, et al. Reproductive age-related changes in the blood-brain barrier: Expression of IgG and tight junction proteins. Microvasc. Res. 2009; 78:413–424. [PubMed: 19591848]

Batoulis H, et al. Experimental autoimmune encephalomyelitis--achievements and prospective advances. APMIS. 2011; 119:819–830. [PubMed: 22085358]

Bechmann I, et al. What is the blood-brain barrier (not)? Trends Immunol. 2007; 28:5–11. [PubMed: 17140851]

Bennett J, et al. Blood-brain barrier disruption and enhanced vascular permeability in the multiple sclerosis model EAE. J Neuroimmunol. 2010; 229:180–191. [PubMed: 20832870]

Bergman CM. A switch in pathogenic mechanism in myelin oligodendrocyte glycoprotein-induced experimental autoimmune encephalomyelitis in IFN-μ-inducible thiol reductase-free mice. J. Immunol. 2012; 188:6001–6009. [PubMed: 22586035]

Berne, RM.; Levy, MN. The Circuitry. Physiology. C.V. Mosby Co.; 1988. p. 395-397.

Blasig IE, Haseloff RF. Tight junctions and tissue barriers. Antioxid Redox Signal. 2011; 15:1163–1166. [PubMed: 21446883]

Brown A, Sawchenko PE. Time course and distribution of inflammatory and neurodegenerative events suggest structural bases for the pathogenesis of experimental autoimmune encephalomyelitis. J. Comp. Neurol. 2007; 502:236–260. [PubMed: 17348011]

Calabria AR, et al. Puromycin-purified rat brain microvascular endothelial cell cultures exhibit improved barrier properties in repsonse to glucocorticoid induction. J. Neurochem. 2006; 97:922–933. [PubMed: 16573646]

Carvey PM, et al. The blood-brain barrier in neurodegenerative disease: a rhetorical perspective. J Neurochem. 2009; 111:291–314. [PubMed: 19659460]

Cavaglia M, et al. Regional variation in brain capillary density and vascular response to ischemia. Brain Res. 2001; 910:81–93. [PubMed: 11489257]

Claudio L, et al. Increased vesicular transport and decreased mitochondrial content in blood-brain barrier endothelial cells during experimental autoimmune encephalomyelitis. Am J Pathol. 1989; 135:1157–1168. [PubMed: 2596575]

Coisne C, Engelhardt B. Tight junctions in brain barriers during central nervous system inflammation. Antioxid Redox Signal. 2011; 15:1285–1303. [PubMed: 21338320]

Dobrogowska DH, Vorbrodt AW. Immunogold localization of tight junctional proteins in normal and osmotically-affected rat blood-brain barrier. J. Mol. Histol. 2004; 35:529–538. [PubMed: 15571330]

Engelhardt B, Sorokin L. The blood-brain and the blood-cerebrospinal fluid barriers: function and dysfunction. Semin. Immunopathol. 2009; 31:497–511. [PubMed: 19779720]

Errede M, et al. Blood-brain barrier alterations in the cerebral cortex in experimental autoimmune encephalomyelitis. J Neuropathol Exp Neurol. 2012; 71:840–854. [PubMed: 23001217]

Fawcett, DW. Bloom and Fawcett A Textbool of Histology. twelfth ed.. New York: Chapman and Hall; 1994.

Fischer S, et al. H_2O_2 induces paracellular permeability of porcine brain-derived microvascular endothelial cells by activation of the p44/42 MAP kinase pathway. Eur J Cell Biol. 2005; 84:687–697. [PubMed: 16106912]

Furuse M. Molecular basis of the core structure of tight junctions. Cold Spring Harb Perspect Biol. 2010; 2:a002907. [PubMed: 20182608]

Garrido-Urbani S, et al. Vascular and epithelial junctions: a barrier for leucocyte migration. Biochem Soc Trans. 2008; 36:203–211. [PubMed: 18363562]

Ge S, et al. Where is the blood-brain barrier … really? J Neurosci Res. 2005; 79:421–427. [PubMed: 15635601]

Gidday JM, et al. Leukocyte-derived matrix metalloproteinase-9 mediates blood-brain barrier breakdown and is proinflammatory after transient focal cerebral ischemia. Am J Physiol Heart Circ Physiol. 2005; 289:H558–H568. [PubMed: 15764676]

Grammas P, et al. Cerebral microvascular endothelium and the pathogenesis of neurodegenerative diseases. Expert Rev Mol Med. 2011; 13:e19. [PubMed: 21676288]

Gruppe TL, et al. The extent of ultrastructural spinal cord pathology reflects disease severity in experimental autoimmune encephalomyelitis. Histol Histopathol. 2012; 27:1163–1174. [PubMed: 22806903]

Gesuete R, et al. Glial cells drive precondtioning-induced blood-brain barrier protection. Stroke. 2011; 42:1445–1453. [PubMed: 21474800]

Haorah J, et al. Ethanol-induced activation of myosin light chain kinase leads to dysfunction of tight junctions and blood-brain barrier compromise. Alcohol Clin Exp Res. 2005; 29:999–1009. [PubMed: 15976526]

Hawkins BT, Davis TP. The blood-brain barrier/neurovascular unit in health and disease. Pharmacol Rev. 2005; 57:173–185. [PubMed: 15914466]

Ishizaki T, et al. Cyclic AMP induces phosphorylation of claudin-5 immunoprecipitates and expression of claudin-5 gene in blood-brain-barrier endothelial cells via protein kinase A-dependent and -independent pathways. Exp Cell Res. 2003; 290:275–288. [PubMed: 14567987]

Ivey NS, et al. Association of FAK activation with lentivirus-induced disruption of blood-brain barrier tight junction-associated ZO-1 protein organization. J Neurovirol. 2009; 15:312–323. [PubMed: 19521898]

Jalali S, et al. Focused ultrasound-mediated BBB disruption is associated with an increase in activation of AKT: experimental study in rats. BMC Neurol. 2010; 10:114. [PubMed: 21078165]

Janacek J, et al. A novel method for evaluation of capillarity in human skeletal muscles from confocal 3D images. Microvasc Res. 2011; 81:231–238. [PubMed: 21145900]

Kreuter J. Mechanism of polymeric nanoparticle-based drug transport across the blood-brain barrier (BBB). J. Microencapsul. 2012

Leeson, RC., et al. Text/Atlas of Histology. Philadelphia: W.B. Saunders Company; 1988.

Liebner S, et al. Current concepts of blood-brain barrier development. Int J Dev Biol. 2011; 55:467–476. [PubMed: 21769778]

Luissint AC, et al. Guanine nucleotide-binding protein G i2: a new partner of claudin-5 that regulates tight junction integrity in human brain endothelial cells. J. Cereb. Blood Metab. 2012; 32:860–873.

Ma T, et al. Evidence for involvement of ROCK signaling in bradykinin-induced increase in murine blood-tumor barrier permeability. J Neurooncol. 2012; 106:291–301. [PubMed: 21892742]

Macdonald JA, et al. Endothelial cell heterogeneity of blood-brain barrier gene expression along the cerebral microvasculature. J Neurosci Res. 2010; 88:1457–1474. [PubMed: 20025060]

Mix E, et al. Animal models of multiple sclerosis--potentials and limitations. Prog Neurobiol. 2010; 92:386–404. [PubMed: 20558237]

Morgan L, et al. Inflammation and dephosphorylation of the tight junction protein occludin in an experimental model of multiple sclerosis. Neuroscience. 2007; 147:664–673. [PubMed: 17560040]

Morin-Brureau M, et al. Epileptiform activity induces vascular remodeling and zonula occludens 1 downregulation in organotypic hippocampal cultures: role of VEGF signaling pathways. J Neurosci. 2011; 31:10677–10688. [PubMed: 21775611]

Morita K, et al. Endothelial claudin: claudin-5/TMVCF constitutes tight junction strands in endothelial cells. J Cell Biol. 1999; 147:185–194. [PubMed: 10508865]

Moxon-Emre I, Schlichter LC. Neutrophil depletion reduces blood-brain barrier breakdown, axon injury, and inflammation after intracerebral hemorrhage. J Neuropathol Exp Neurol. 2011; 70:218–235. [PubMed: 21293296]

Murugesan N, et al. Active induction of experimental autoimmune encephalomyelitis by MOG35-55 peptide immunization is associated with differential responses in separate compartments of the choroid plexus. Fluids Barriers CNS. 2012; 9:15. [PubMed: 22870943]

Nakagawa S, et al. A new blood-brain barrier model using primary rat brain endothelial cells, pericytes and astrocytes. Neurochem. Internatl. 2009; 54:253–263.

Nagy Z, et al. Fracture faces of cell junctions in cerebral endothelium during normal and hyperosmotic conditions. Lab Invest. 1984; 50:313–322. [PubMed: 6422163]

Nitta T, et al. Size-selective loosening of the blood-brain barrier in claudin-5-deficient mice. J Cell Biol. 2003; 161:653–660. [PubMed: 12743111]

Ohtsuki S, et al. Exogenous expression of claudin-5 induces barrier properties in cultured rat brain capillary endothelial cells. J Cell Physiol. 2007; 210:81–86. [PubMed: 16998798]

Owens T, et al. Perivascular spaces and the two steps to neuroinflammation. J. Neuropathol. Exp. Neurol. 2008; 67:1113–1121. [PubMed: 19018243]

Pachner AR. Experimental models of multiple sclerosis. Curr. Opin. Neurol. 2011; 24:291–299. [PubMed: 21519255]

Paolinelli R, et al. The molecular basis of the blood-brain barrier differentiation and maintenance. Is it still a mystery? Pharmacol Res. 2011; 63:165–171. [PubMed: 21167284]

Persidsky Y, et al. Rho-mediated regulation of tight junctions during monocyte migration across the blood-brain barrier in HIV-1 encephalitis (HIVE). Blood. 2006; 107:4770–4780. [PubMed: 16478881]

Petty MA, Lo EH. Junctional complexes of the blood-brain barrier: permeability changes in neuroinflammation. Prog Neurobiol. 2002; 68:311–323. [PubMed: 12531232]

Pfeiffer F, et al. Claudin-1 induced sealing of blood-brain barrier tight junctions ameliorates chronic experimental auotimmune encephalomyelitis. Acta Neuropathol. 2011; 122:601–614. [PubMed: 21983942]

Pober JS, Sessa WC. Evolving functions of endothelial cells in inflammation. Nat Rev Immunol. 2007; 7:803–815. [PubMed: 17893694]

Proulx DP, et al. Interaction between intravenous immunoglobulin (IVIg) and the low-density lipoprotein receptor-related protein 1: A role for transcytosis across the blood brain barrier? J Neuroimmunol. 2012; 251:39–44. [PubMed: 22796178]

Pun PB, et al. Involvement of ROS in BBB dysfunction. Free Radic Res. 2009; 43:348–364. [PubMed: 19241241]

Ross, MH.; Pawlina, W. Histology: A Text and Atlas. fifth ed.. Baltimore: Lipincott Williams and Wilkins; 2006.

Saubamea B, et al. Heterogeneity in the rat brain vasculature revealed by quantitative confocal analysis of endothelial barrier antigen and P-glycoprotein expression. J Cereb Blood Flow Metab. 2012; 32:81–92. [PubMed: 21792241]

Sheikov N, et al. Effect of focused ultrasound applied with an ultrasound contrast agent on the tight junctional integrity of the brain microvascular endothelium. Ultrasound Med. Biol. 2008; 34:1093–1104. [PubMed: 18378064]

Simionescu, N.; Simionescu, M. The cardiovascular system. In: Weiss, L.; Greep, RO., editors. Histology. McGraw Hill; New York: 1077. p. 373-431.

Sixt M, et al. Endothelial cell laminin isoforms, laminins 8 and 10, play decisive roles in T cell recruitment across the blood-brain barrier in experimental autoimmune encephalomyelitis. J Cell Biol. 2001; 153:933–946. [PubMed: 11381080]

Song L, Pachter JS. Culture of murine brain microvascular endothelial cells that maintain expression and cytoskeletal association of tight junction-associated proteins. In Vitro Cell. Devel. Biol. Animal. 2003; 39:313–320.

Song L, Pachter JS. Monocyte chemoattractant protein-1 alters expression of tight junction-associated proteins in brain microvascular endothelial cells. Microvasc Res. 2004; 67:78–89. [PubMed: 14709405]

Suen WE, et al. A critical role for lymphotoxin in experimental allergic encephalomyelitis. J. Exp. Med. 1997; 189:1233–1240. [PubMed: 9334362]

Suidan GL, et al. Induction of blood brain barrier tight junction protein alterations by CD8 T cells. PLoS One. 2008; 3:e3037. [PubMed: 18725947]

Thurston G, et al. Determinants of endothelial cell phenotype in venules. Microcirculation. 2000; 7:67–80. [PubMed: 10708338]

van Horssen J, et al. Basement membrane proteins in multiple sclerosis-associated inflammatory cuffs: potential role in influx and transport of leukocytes. J Neuropathol Exp Neurol. 2005; 64:722–729. [PubMed: 16106221]

Vorbrodt AW, et al. Ultrastructural localization of lectin receptors on the luminal and abluminal aspects of brain micro-blood vessels. J Histochem Cytochem. 1986; 34:251–261. [PubMed: 3753715]

Ward R, et al. A quantitative study of cerebrovascular variation in inbred mice. J Anat. 1990; 173:87–95. [PubMed: 2074233]

Wolburg H, et al. Localization of claudin-3 in tight junctions of the blood-brain barrier is selectively lost during experimental autoimmune encephalomyelitis and human glioblastoma multiforme. Acta Neuropathol. 2003; 105:586–592. [PubMed: 12734665]

Xu H, et al. J. Leukocyte diapedesis in vivo induces transient loss of tight junction protein at the blood-retina barrier. Invest Ophthalmol Vis Sci. 2005; 46:2487–2494. [PubMed: 15980240]

Xu H, Liversidge J. Quantitative in situ analysis of claudin expression at the blood-retinal barrier. Methods Mol Biol. 2011; 762:321–331. [PubMed: 21717367]

Zhong Y, et al. Caveolin-1 regulates human immunodeficiency virus-1 Tat-induced alterations of tight junction protein expression via modulation of the Ras signaling. J Neurosci. 2008; 28:7788–7796. [PubMed: 18667611]

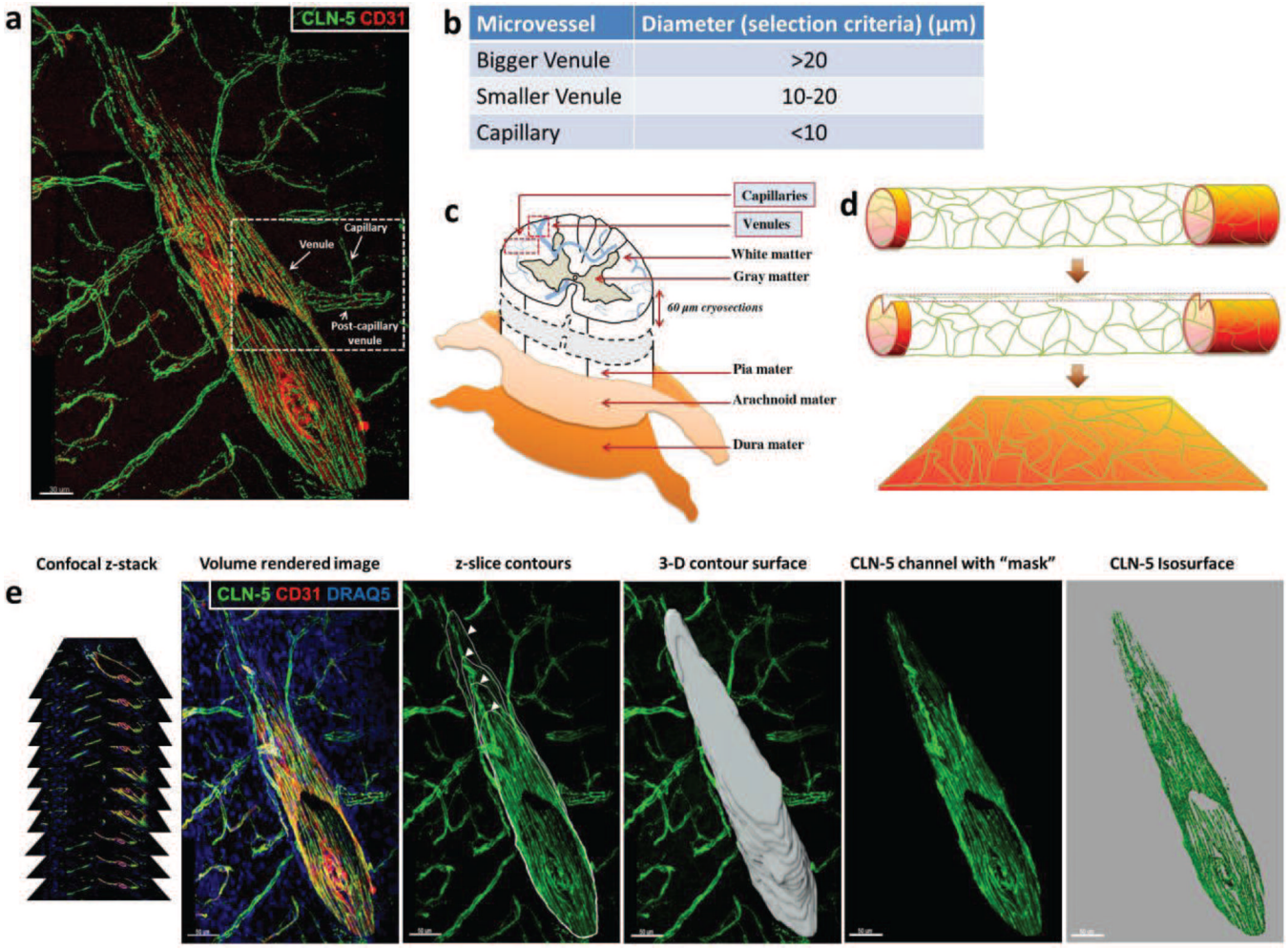

Fig. 1. 3D Contour-based quantification of junctional CLN-5 in spinal cord microvessels

(a) CNS venule from a naïve mouse detailing CLN-5 (Green) staining at intercellular junctions. The image shows microvascular tributaries (e.g. capillaries, post-capillary venules) emerging from a venule, whose lumen has been "optically" cut open to reveal the inner vessel wall. Endothelial cells are highlighted with CD31 (Red). **(b,c)** To gauge endothelial heterogeneity with respect to CLN-5, spinal cord microvessels (capillaries and venules) obtained in confocal z-stacks from the dorsolateral white matter (between T10 and L3 vertebrae) were imaged and categorized into appropriate segments based on their average diameter. **(d)** Schematic indicating this method effectively allows the surface area of the microvascular endothelium to be spread out in 3D space (x, y, z axes) for quantification of CLN-5 density per unit area, while excluding the luminal volume. **(e)** To quantify CLN-5 staining associated with a microvessel in 3D, an individual contour for each confocal z-slice was created by cursoring out the vessel of interest, and the individual z-slice contours then merged into a 3D contour surface. This contour surface was utilized to isolate the microvessel of interest from the rest of the dataset (masking), and its area was used as an estimate of the "microvascular surface area" defined by the endothelial layer. An isosurface for the CLN-5 channel was then created from the selected vessel for statistical analysis. Scale bar = 50μm.

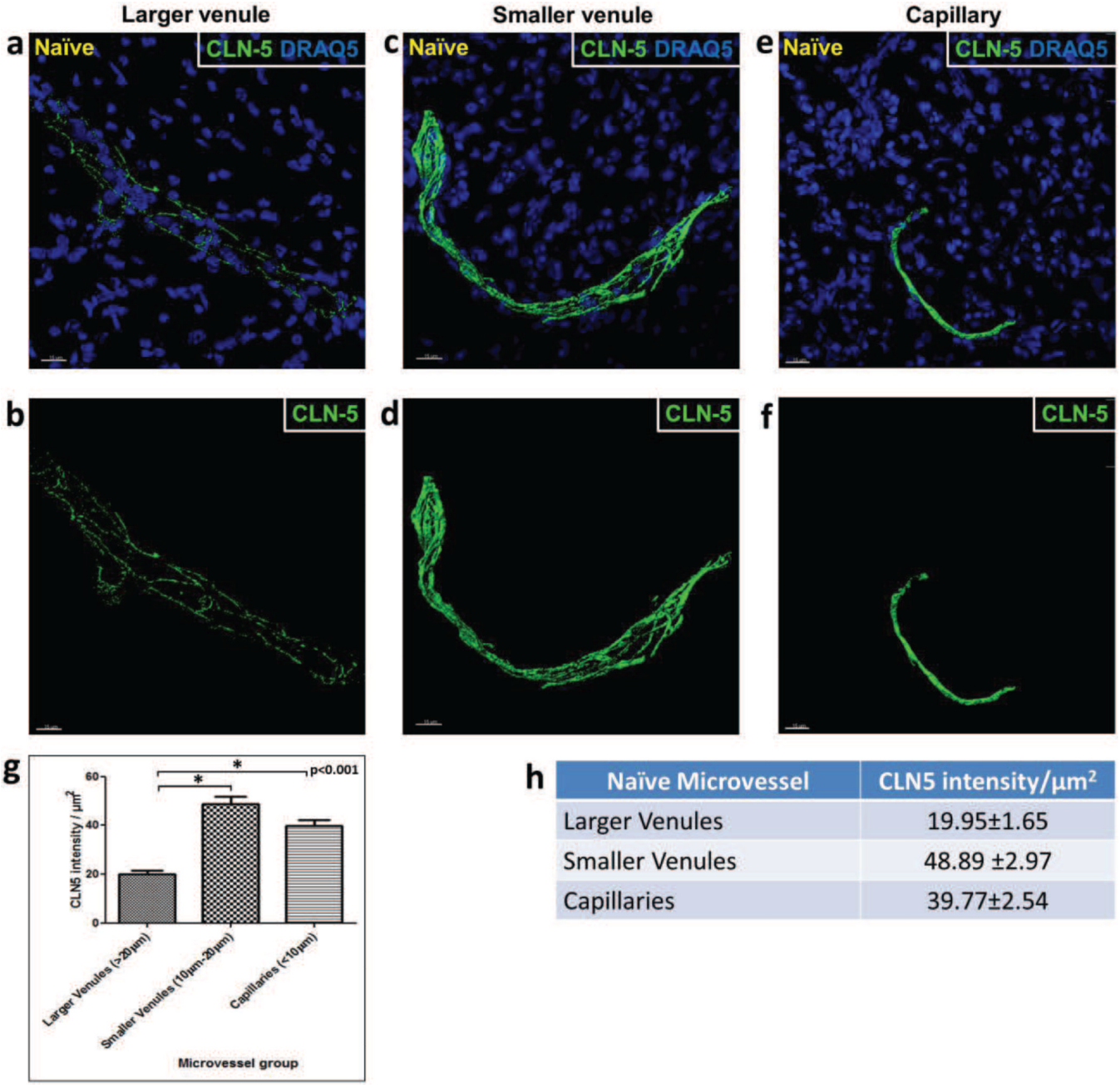

h

Naïve Microvessel	CLN5 intensity/µm²
Larger Venules	19.95±1.65
Smaller Venules	48.89 ±2.97
Capillaries	39.77±2.54

Fig. 2. Heterogeneity in CLN-5 density distribution among different-sized microvessels in naïve spinal cord

Isosurface rendering of the CLN-5 channel was performed in confocal z-stacks of different-sized spinal cord microvessels in tissue sections from naïve mice: **(a,b)** larger venules; **(c,d)** smaller venules; **(e,f)** capillaries. Top row, shows CLN-5 (Green) and nuclei/DRAQ5 (Blue). Bottom row, shows CLN-5 only, to emphasize the disparity in junctional CLN-5 immunostaining between the smaller and larger microvessels. **(g,h)** 3D contour-based quantification of CLN-5 density (intensity per unit surface area of the endothelium) within naïve spinal cord microvessels. Junctional CLN-5 density was greatest in the capillaries and smaller venules, and least in the larger venules. A total of 5 microvessels were analyzed in each group sampled from 3 mice. $*p < 0.001$. Scale bar = 15µm.

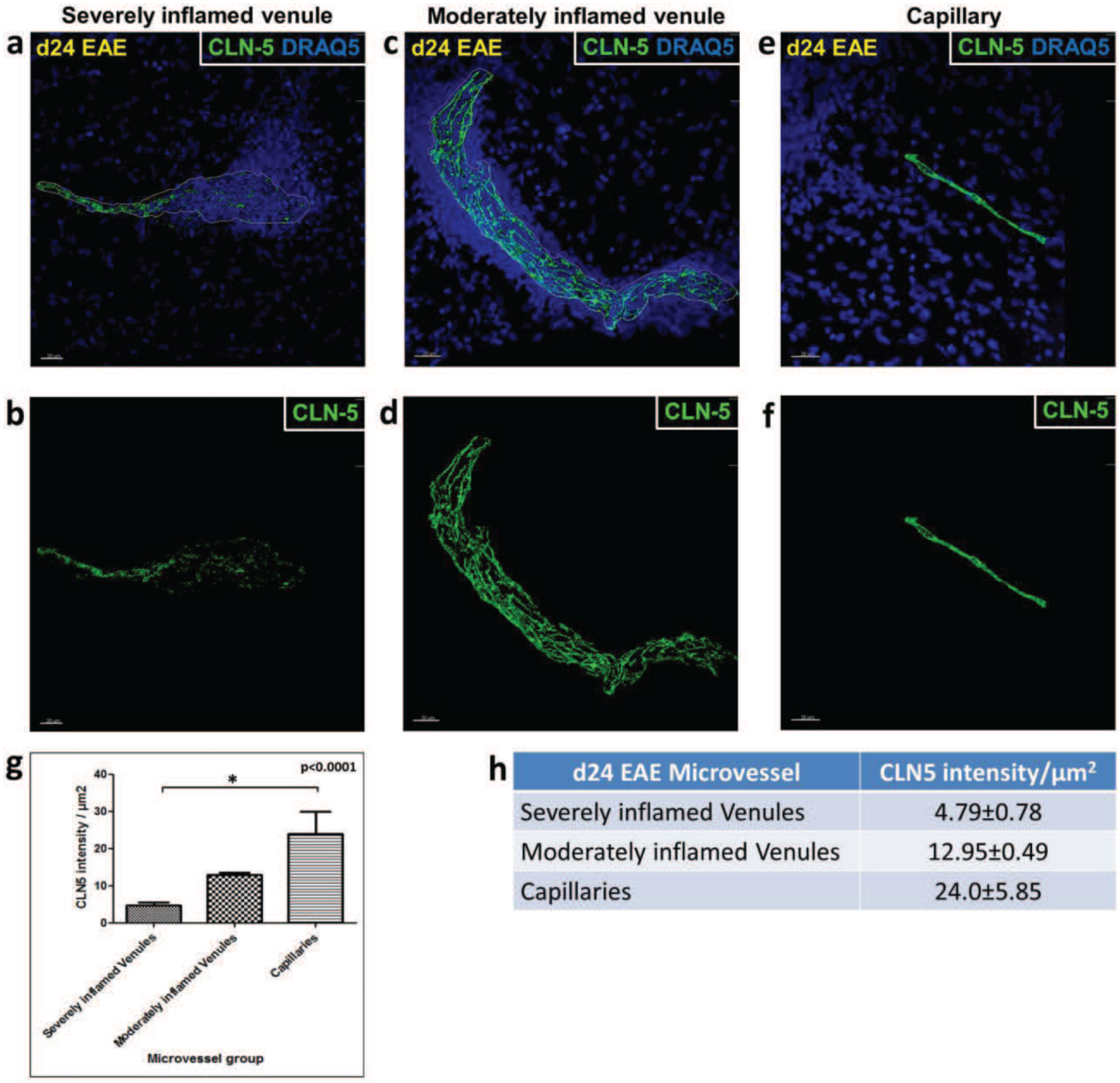

h

d24 EAE Microvessel	CLN5 intensity/µm²
Severely inflamed Venules	4.79±0.78
Moderately inflamed Venules	12.95±0.49
Capillaries	24.0±5.85

Fig. 3. CLN-5 density in spinal cord microvessels during EAE

Isosurface rendering of the CLN-5 channel was performed in confocal z-stacks of spinal cord microvessels at d24 EAE. Top row, shows CLN-5 (Green) and nuclei/DRAQ5 (Blue) to highlight the close association of altered CLN-5 with dense perivascular cellularity. Bottom row, shows staining of only CLN-5 to emphasize significant TJ protein disruption. Inflamed venules demonstrated heterogeneity in CLN-5 loss: **(a,b)** severely inflamed venules displayed diffuse and extensive disruption of CLN-5; **(c,d)** moderately inflamed venules showed small punctate regions of CLN-5 loss; and **(e,f)** capillaries adjacent to severely inflamed venules appeared refractory to CLN-5 loss. 3D quantification of intercellular CLN-5 staining showed a significant reduction in intensity of CLN-5 staining per unit area of the endothelium in the severely inflamed venules compared to the capillaries

(g,h). The boundaries of inflamed venules are marked with dashed white lines. A total of 6 microvessels were analyzed in each group sampled from 3 mice. *$p < 0.0001$. Scale bar = 20μm.

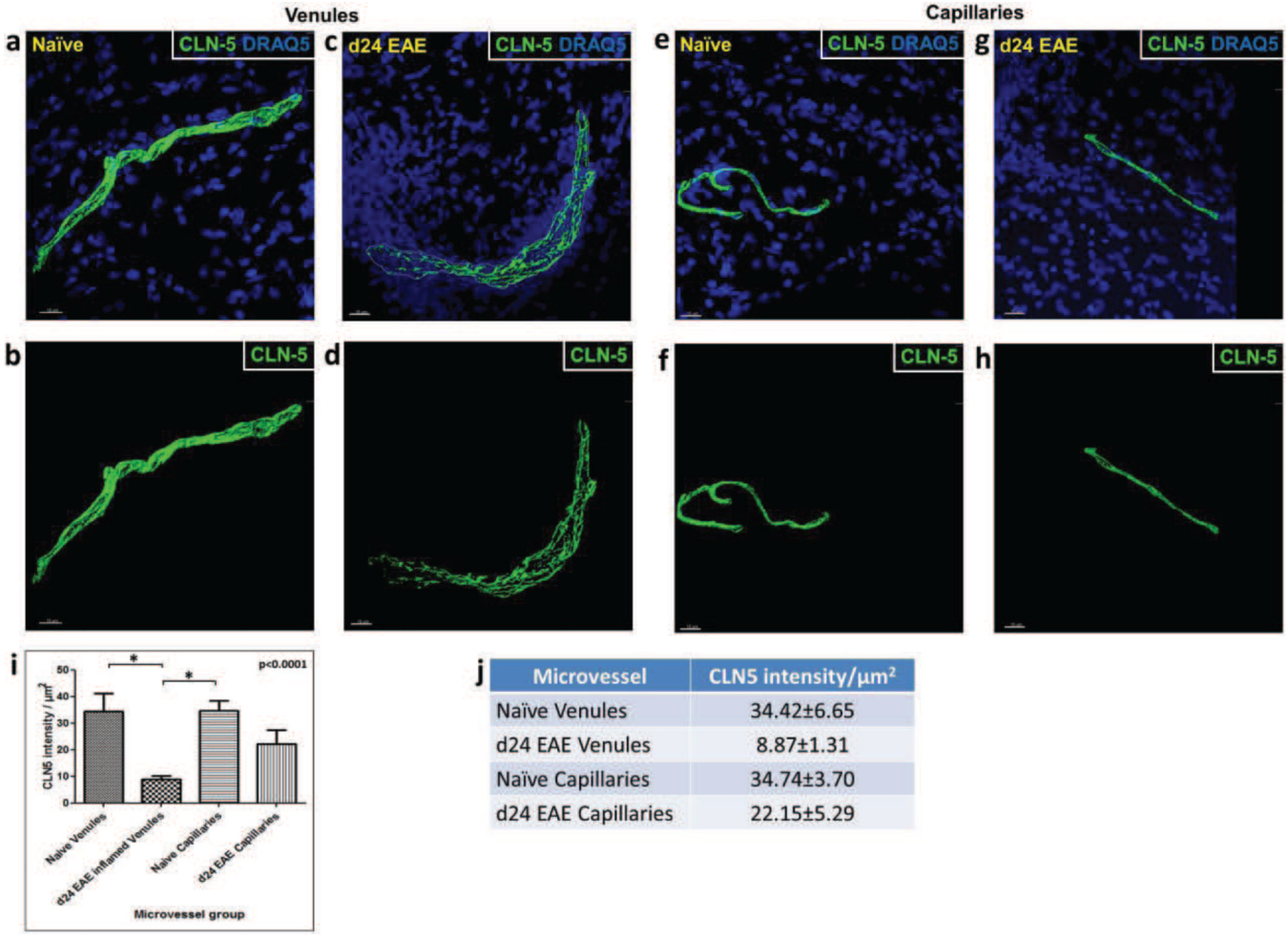

Microvessel	CLN5 intensity/µm²
Naïve Venules	34.42±6.65
d24 EAE Venules	8.87±1.31
Naïve Capillaries	34.74±3.70
d24 EAE Capillaries	22.15±5.29

Fig. 4. CLN-5 density in spinal cord microvessels from naïve vs. EAE mice

Isosurface rendering of z-stacked images of spinal cord sections from naïve mice and mice at d24 EAE. Top row, shows staining of CLN-5 (Green) and DRAQ5 (Blue) to highlight the close association of altered CLN-5 with dense perivascular cellularity (reflective of leukocyte infiltrates) during EAE. Bottom row, shows staining of only CLN-5 to emphasize significant TJ protein disruption that accompanies disease. **(a,b)** Venules from naïve mice; **(c,d)** Venules from d24 EAE mice; **(e,f)** Capillaries from naïve mice; and **(g,h)** Capillaries from d24 EAE mice. **(i,j)** 3D quantification of CLN-5 microvascular staining showed a significant reduction in CLN-5 density in inflamed venules compared to the naïve venules and naïve capillaries. The boundary of inflamed venule is marked with dashed white line. A total of 6 microvessels were analyzed in each group sampled from 3 mice. $*p < 0.0001$. Scale bar = 15µm.

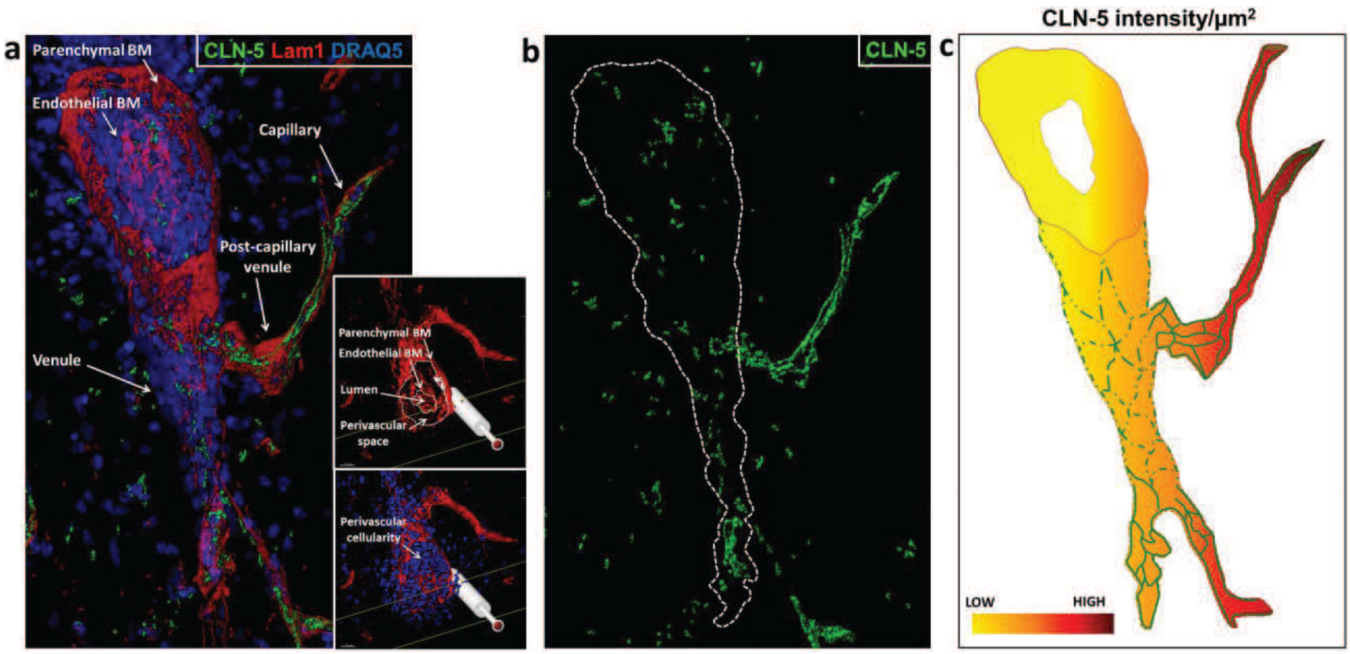

Fig. 5. Heterogeneity in CLN-5 density in a contiguous venule/capillary pair during EAE

(a) Isosurface rendered 3D reconstruction of a contiguous venule and capillary in spinal cord section from d24 EAE mouse, highlighting basement membrane/Lam1 (Red), CLN-5 (Green), and nuclei/DRAQ-5 (Blue). **(b)** Isosurface rendered CLN-5 channel only, with boundary of the inflamed venule marked with dashed white line. The venule shows severe loss and fragmentation of junctional CLN-5, while the attached capillary displays intact junctional CLN-5 staining. The insets reveal cross sections through the inflamed venule, optically cut using clipping plane module in Imaris®, demonstrating association of venular CLN-5 loss with seminal signs of inflammation: (top) separation of endothelial and astrocyte basement membranes (BM); and (bottom) increased perivascular cellularity. **(c)** Schematic representation showing, qualitatively, heterogeneity in CLN-5 density distribution in a contiguous venule/capillary pair at d24 EAE.

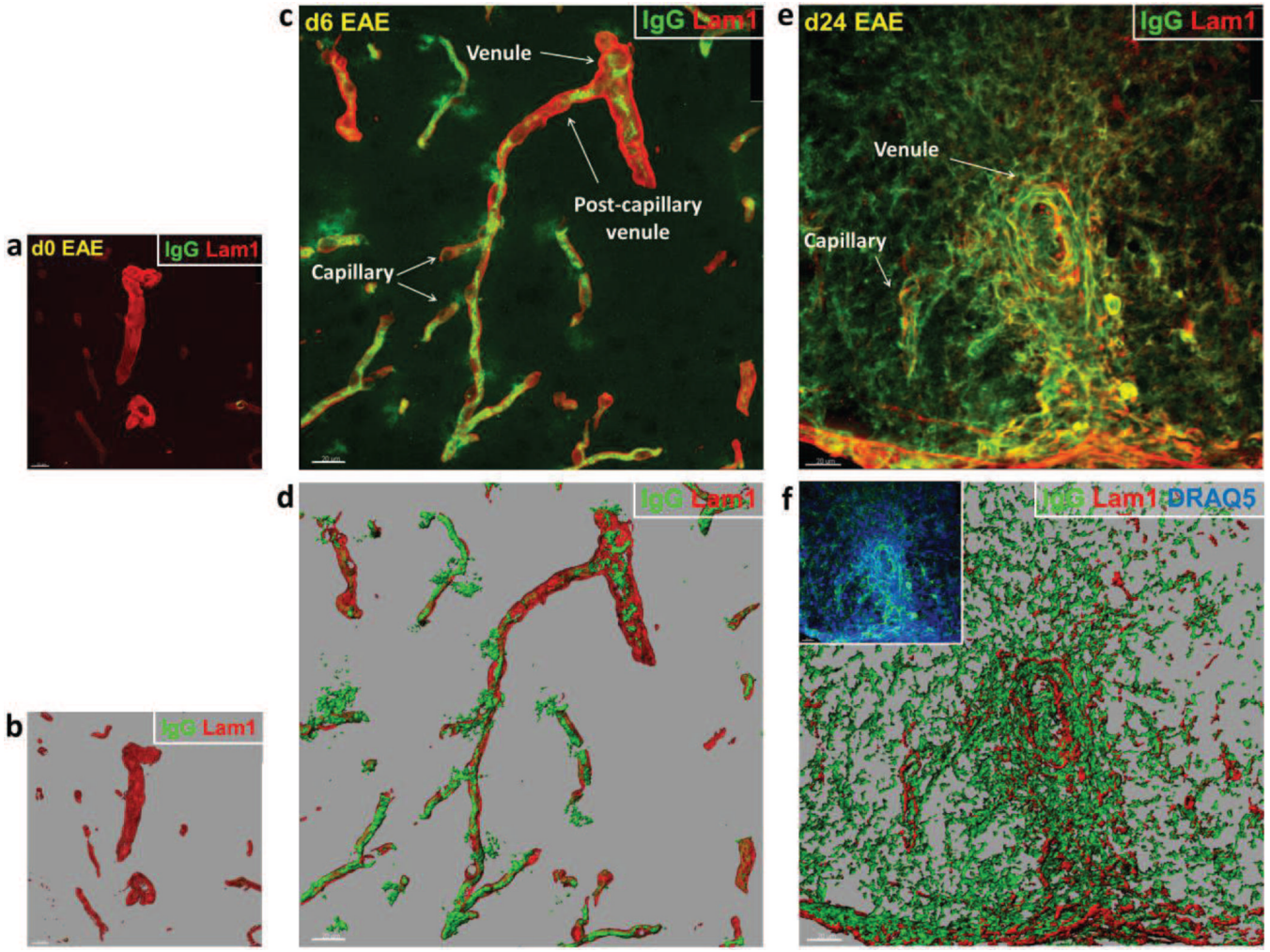

Fig. 6. Endogenous serum IgG leakage from spinal cord microvessels during EAE

(a,c,e) Shows volume rendered images of confocal z-stacks from microvascular segments obtained from naïve mice, and mice at d6 and d24 EAE. **(b,d,f)** Shows the corresponding isosurface rendered images for purpose of enhanced spatial perspective. Staining of IgG (Green) and basement membrane/LAM 1 (Red) highlights vascular permeability around venules and capillaries. **(a,b)** Microvessels from naïve mice reveal no visible IgG immunostaining associated with venules or capillaries. **(c,d)** Microvessels at d6 EAE – prior to evidence of clinical disease – display focal IgG immunoreactivity around both venules and capillaries. **(e,f)** Microvessels at d24 EAE show pronounced and diffuse IgG immunoreactivity – reflecting endogenous serum protein extravasation – which obscured boundaries between the microvessel segments. Increased perivascular cellularity, indicative of leukocyte infiltration (inset), is highlighted by DRAQ5 staining (Blue). Scale bar = 20μm.